Atmospheric Research 120–121 (2013) 216–225

Contents lists available at SciVerse ScienceDirect

Atmospheric Research

journal homepage: www.elsevier.com/locate/atmos

Orographic effects related to deep convection events over the Andes region

R. Hierro [a,*], H. Pessano [b], P. Llamedo [a], A. de la Torre [a], P. Alexander [c], A. Odiard [d]

[a] Facultad de Ingeniería, Universidad Austral, Avda. J. de Garay 125, C1063ABB Buenos Aires, Argentina
[b] Facultad Regional San Rafael, Universidad Tecnológica Nacional, Avda. Urquiza 314, M5602GCH San Rafael, Mendoza, Argentina
[c] Departamento de Física, FCEN, Universidad de Buenos Aires, Ciudad Universitaria, C1428EGA Buenos Aires, Argentina
[d] Dirección de Agricultura y Contingencias Climáticas, Gobierno de Mendoza, San Martín 1850, M5560EWS Mendoza, Argentina

ARTICLE INFO

Article history:
Received 10 April 2012
Received in revised form 28 August 2012
Accepted 30 August 2012

Keywords:
Mountain waves
Storms
Andes
Mendoza

ABSTRACT

In this work, we analyze a set of 39 storms which took place between 2006 and 2011 over the South of Mendoza, Argentina. This is a semiarid region situated at mid-latitudes (roughly between 32S and 36S) at the east of the highest Andes tops which constitutes a natural laboratory where diverse sources of gravity waves usually take place. We consider a cultivated subregion near San Rafael district, where every summer a systematic generation of deep convection events is registered. We propose that the lift mechanism required to raise a parcel to its level of free convection is partially supplied by mountain waves (MWs). From Weather Research and Forecasting (WRF) mesoscale model simulations and radar network data, we calculate the evolution of convective available potential energy and convective inhibition indices during the development of each storm. Global Final Analysis is used to construct initial and boundary conditions. Convective inhibition indices are compared with the vertical kinetic energy capable of being supplied by the MWs, in order to provide a rough estimation of this possible triggering mechanism. Vertical velocity is chosen as an appropriate dynamical variable to evidence the presence of MWs in the vicinity of each detected first radar echo. After establishing a criterion based on a previous work to represent MWs, the 39 storms are split into two subsets: with and without the presence of MWs. 12 cases with considerable MWs amplitude are retained and considered. Radar data differences between the two samples are analyzed and the simulated MWs are characterized.

1. Introduction

Unstable tropospheric conditions are necessary to allow the rising of an air parcel and develop deep convection. These situations have been evaluated for many years through the use of several indices. The K-index was defined by George (1960) to forecast the occurrence of thunderstorms over the east of the United States and southeastern Canada. Miller (1967) devised the Total Totals index to locate potential severe weather development in the United States. The Showalter index (Showalter, 1953) was designed for the forecasting of thunderstorms in the southwestern United States. The Lifted Index was developed by Galway (1956) and quantifies the difference between a given saturated parcel temperature and the 500 hPa environmental temperature. Although it is not a true measure of instability, Moncrieff and Miller (1976) named convective available potential energy (*CAPE*) the integrated effect of the positive buoyancy of the rising undiluted parcel relative to its environment (e.g. Williams and Renno, 1992; Emanuel, 1994). On the other hand, the convection inhibition (*CIN*) index equals the negative work done by the boundary layer parcel as it rises through the stable layer to its level of free convection (Colby, 1984). Johns and Doswell (1992) stated that convection may be triggered by the combination of factors such as diurnal warming, orographic lifting and upward motion over a frontal zone. However, it is well known that the convection over complex terrain regions is generated by a still more complicated mechanism, possibly involving additional forcings or a combination of them (Houze, 1993). It is often necessary to

* Corresponding author.
E-mail address: rhierro@austral.edu.ar (R. Hierro).

0169-8095/$ – see front matter © 2012 Elsevier B.V. All rights reserved.
http://dx.doi.org/10.1016/j.atmosres.2012.08.020

distinguish such forcings in order to produce a good forecast at a given place (López et al., 2007). One of the most important effects of the severe storms is the hail production, which may cause important damages to the local population in general. Sánchez et al. (1999) stated that two ingredients are required for the hail formation: supercooled liquid water and sufficient updraft. With respect to hail detection, Fraile et al. (2001) found that the maximum reflectivity, the top of the cell and the height of the maximum reflectivity are significantly different in hail and no-hail storms, while López and Sánchez (2009) pointed out that the high values of reflectivity are found when high values of liquid water are present. Lemon (1980) suggested that a storm which exceeds 50–57 dBz would be severe, depending on the time of year while Donavon and Jungbluth (2007) focused upon the height of the 50 dBz reflectivity echo and its usefulness as an indicator for severe hail potential.

The eastern side of the Andes mid-latitudes between the subtropical and polar jets (Houze, 2012), where a considerable number of N–S aligned deep valleys are present over the Mendoza region (Argentina; 32–36S, 70–67W), deserves particular attention. Brooks et al. (2003) pointed out that Argentina belongs to a South American region where favorable conditions for the occurrence of severe hailstorms during the austral summer are usually found. Sánchez et al. (2008) found that between 1984 and 2004, an average of 68 days with storm cells were registered with reflectivities over 55 dBz. 60% of these cases occurred during the austral summer (December, January and February). García-Ortega et al. (2009) pointed out that from October to April, between 1994 and 2006, an average of 128 storm days was registered. They presented reflectivity factors (Z) over 45 dBZ and in 118 cases at least one storm cell had a reflectivity factor of 55 dBZ. However, only a few authors have studied some dynamic processes involving the development of strong convection events over this region: de la Torre et al. (2004), combining radar analysis, satellite, radiosonde data and numerical simulations, found that a deep convection event was generated because of the simultaneous presence of anabatic winds as the triggering mechanism, an accumulation of moist enthalpy and sufficient instability conditions. García-Ortega et al. (2009) presented two hailstorm case studies and found that the diurnal temperatures and the regional topography favored convection, suggesting that the Andes Mountains and solar radiation could have played a key role in triggering them. De la Torre et al. (2011) studied three cases of severe storms with hail production, finding a relationship between MWs and the development of deep convection. Taking into account that vertical velocity (w) constitutes an appropriate dynamical variable to evidence the presence of MWs (e.g. Smith, 1979; Shutts et al., 1988), de la Torre et al. (2011) studied three storm events over this region, concluding that MWs could represent the main forcing for these cases: *CAPE* and *CIN* indices were analyzed, concluding that *CAPE* grew with decreasing *CIN* and increasing time until deep convection development has been clearly established. In that context, the mechanical forcing provided by the MWs was estimated as sufficient to trigger deep convection for the three cases considered. Several authors (e. g. Eckermann and Preusse, 1999; de la Torre et al., 2006) pointed out that high and middle intrinsic frequency MWs are permanently generated over Mendoza. MWs in the horizontal wavelength range of 20–140 km were identified by de la Torre et al. (2011). The aim of this paper is (i) to determine basic features of the storm events observed at mid-latitudes over the eastern side of the Andes, in presence or absence of MWs during its convection development and (ii) to evaluate the role of the MWs as a trigger mechanism and to characterize the waves present. In Section 2, the employed data and the following methodology are described. In Section 3, we present the results from radar data and numerical simulations. The detected MWs and the observed storms are characterized. Finally, in Section 4, some conclusions are outlined.

2. Data set and methodology

2.1. Numerical simulations

From Weather Research and Forecasting (WRF 3.0) regional model (Skamarock et al., 2008), the regional circulation previous to the deep convection events and, in particular, w and temperature (T) fields before and during the development of these events was determined. The simulations were performed using the $1\times1°$ National Center of Environmental Prediction (NCEP) Global Final Analysis (FNL) to construct initial and boundary conditions. The simulations were carried out in three nested domains, with 43 vertical levels and a 24 s time step for the highest resolution domain. Soil parameters use the same NCEP FNL data. The three domains selected have horizontal resolutions of 36 km (2500×2500 km extent), 12 km (1044×1080 km extent) and 4 km (456×564 km extent), respectively, covering areas with vertices ranging respectively from (83W, 18S) to (56W, 45S), (75W, 39S) to (64W, 27S) and (72W, 36S) to (67W, 31S) (inner domain). The schemes used for the three domains were the following: WRF Single Moment-6 class (WSM6; Hong et al., 2004); Yonsei University PBL (YSU; Hong et al., 2006) to represent the planetary boundary-layer physics; Rapid Radiative Transfer Model Longwave (RRTM; Mlawer et al., 1997) and MM5 Dudhia Shortwave (Dudhia scheme; Dudhia, 1989) for radiation processes; the Noah land surface model (developed jointly by NCAR and NCEP; Skamarock et al., 2008) and Monin–Obukhov scheme (Monin and Obukhov, 1954) for surface physics and thermal diffusion processes, respectively. The cumulus parameterization used was the New Grell scheme (Grell 3; Grell and Devenyi, 2002) for the first and second domains while no-cumulus parameterization was selected for the inner domain. Fig. 1 shows the three domains employed to perform the simulations. The inner domain shows the orography (shaded) and the three cultivated oasis regions in Mendoza. The southern oasis includes San Rafael city. This study considers case studies belonging only to this oasis.

2.2. Radar data

The Mendoza region is covered by a three-conventional weather radar network consisting in two S-bands situated at (34.6S, 68.0W) and (33.0S, 68.4W) ($\lambda = 10.4$ cm) and one C-band ($\lambda = 2.99$ cm), situated at (34.3S, 69.3W). The radar network data are integrated using the Thunderstorm Identification Tracking Analysis and Nowcasting (TITAN; Dixon and Wiener, 1993) radar software which provides composite images selecting the maximum values in overlapping areas. The TITAN application identifies storm cells in volumetric

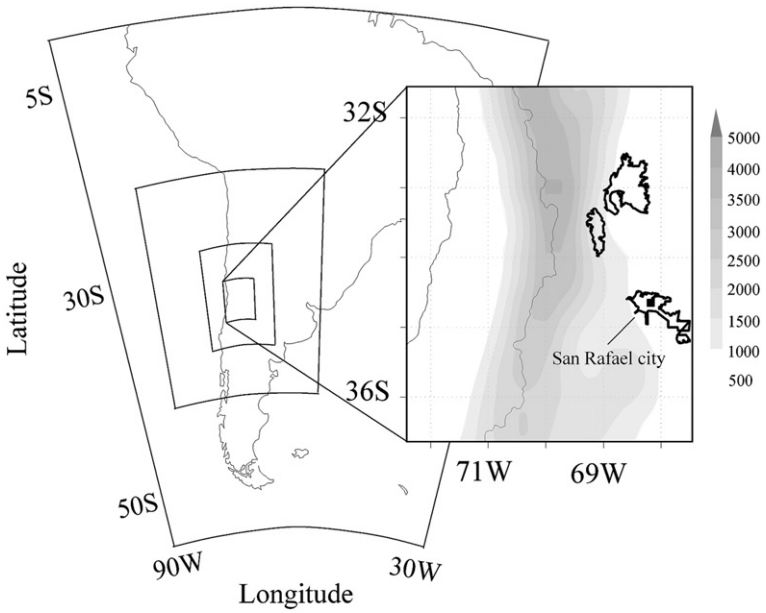

Fig. 1. The three domains selected in the simulations. Topography and the three cultivated areas in the inner domain.

radar data with a 1 km^3 spatial resolution, tracking their evolution. A "storm" was defined as a three-dimensional region for which the radar reflectivity and volume exceed defined thresholds. Following Dixon and Wiener (1993), operational thresholds are set to 35 dBz for reflectivity and 50 km^3 for the volume. Frequently, two or more convective storms merge to form a single storm, or a single storm splits into two or more. In these cases, a manual tracking was performed. The direction and speed of displacement of each cell were calculated from the reflectivity-weighted centroid and the volumetric-scan time interval (≈4 min). 404 convective storms were detected in the Mendoza region during the October–March seasons from 2006 to 2011. From these, 119 (~29.4%) convective storms reached the southern cultivated area and 39 (~9.6%) caused severe damage to the agriculture activity. The damage inside the cultivated area is verified, georeferenced and compared with the TITAN tracking by the Dirección de Agricultura y Contingencias Climáticas (DACC). Additionally, a 200-hailpads network, regularly spaced every 5 km inside the cultivated area, is used to verify the hail tracks described by TITAN. The considered 39 convective storms arrived in San Rafael city (see following section). When the operational threshold is first exceeded, the TITAN shows the first radar echo (hereinafter FRE) corresponding to each storm. The time of development (FRE) is normalized to zero ($t=0$), considering one hour intervals.

2.3. Detection of MWs

Among the 39 selected storms, the simulated w fields are used to analyze the possible presence of MWs in the vicinity of each FRE cell. The background of w is removed applying a band-pass filter between 20 and 240 km to obtain w', retaining only wavelengths belonging to typical MWs in the region (de la Torre et al., 2006). Due to the 3-D nature of gravity waves, it is possible to perform a wave analysis along horizontal, vertical or slanted directions (i.e. de la Torre et al., 2011). In this case, the regional configuration is dominated by an almost meridionally aligned orography with predominant westerly winds. This allows to study MWs along constant latitude bands at the position of each FRE. Based on both the intensity and horizontal extension of w', we applied the following criteria to identify MWs: (i) in a 100 km radius region including each FRE, an area where $|w'|>0.5$ m/s at 600 hPa level exceeded 200 km^2 during at least 6 h previous to each FRE and (ii) a time-constant behavior of w' should be clear during the same period. The analysis is carried out at the average mountain tops height in this region (≈600 hPa). As a result, we retain 12 cases that satisfy these last requirements. The 39 storms originally selected in the southern cultivated area may be split in two subsets: with and without the presence of MWs. Hereinafter, we refer to the MWs and no MWs events sample as M_w and NoM_w, respectively.

3. Results

3.1. FRE and modeled ascent

From the 39 selected storms, colored cells in Fig. 2a show the predominant observed FRE zones specifying the number of storms that took place in each cell. Storm geneses are spread along the west of San Rafael that almost aligned with the regional topography (contours), which presents a systematic decrease towards the east. The eastern downslope with respect to the main synoptic flow seems to constitute a favored zone to generate convection. Fig. 2b shows the modeled maximum w' values found from simulations. Coinciding with the most frequent geneses locations (Fig. 2a), a maximum zone above the lee side of the 1500 m isoline is found. In the concavity of the orography a maximum core is located, favoring the upstream convergence (Schneidereit and Schär, 1999; Miglietta and Buzzi, 2004). Cells with maximum w' follow the mountain relief, acquiring a meridional distribution between 34S and 36S,

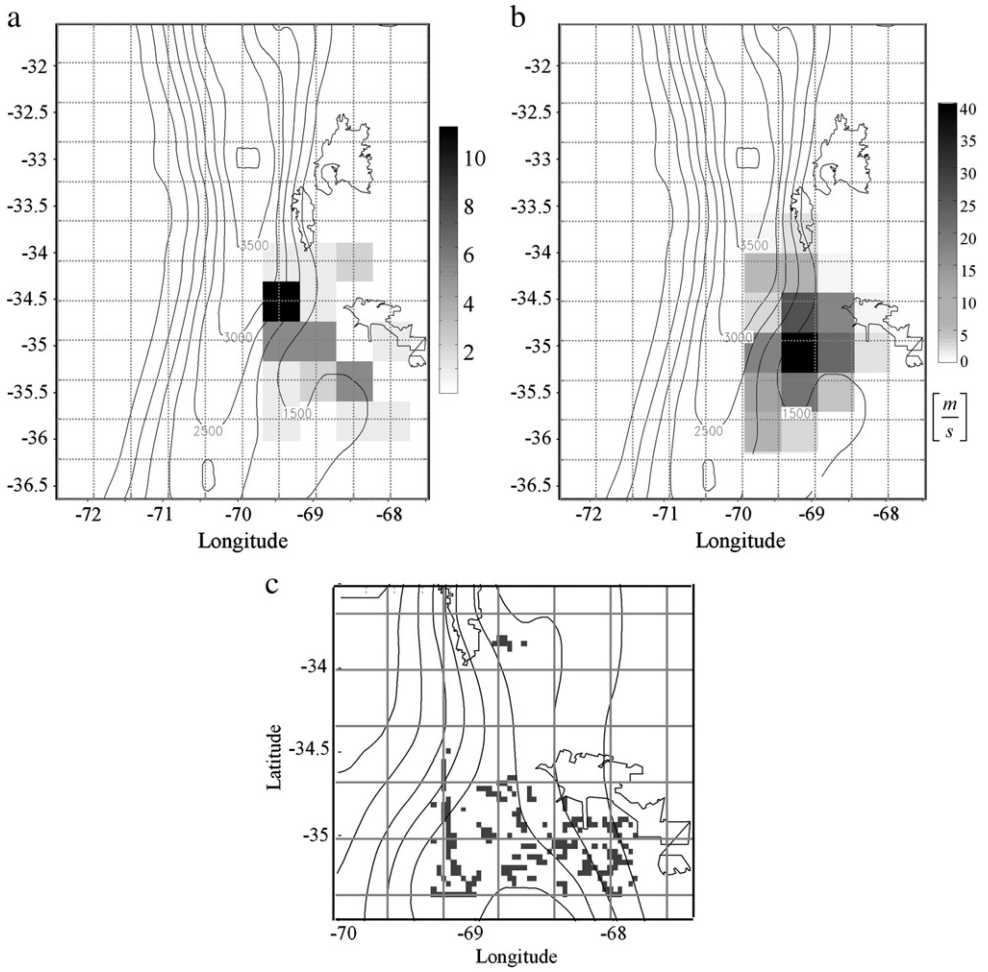

Fig. 2. a) FRE locations in cells of 40×40 km over the third domain (see Fig. 1) for the 39 cases; b) accumulated maximum of w' taken in 40×40 km cells in order to present the influenced area, over the same region for the 39 cases; c) $FACD>0$ (see text) averaged for all cases at the FRE time. Contours indicate the terrain height.

with maximum density at the center of this region. We evaluate the model capability to reproduce the FRE zones following the procedure employed by García-Ortega et al. (2009). They selected the areas with favorable conditions for the storms formation checking the Favorable Area for Convection Development (FACD) index, which is obtained by combining the following parameters: the water vapor flux divergence averaged in the layer 1000–700 hPa (WVFD), the vertical velocity at 700 hPa (w_{700}), and the convective instability (CI) in the layer 900–700 hPa ($\theta_e^{700}-\theta_e^{900}$). Positive values of FACD indicate the joint occurrence of $WVFD<0$, $w_{700}>0$ and $CI<0$. Fig. 2c shows the accumulated $FACD>0$ for all cases with a 4×4 km resolution over the study region. As an indication that the model is able to detect deep convection events, favorable areas for convection development are present above the southern region, roughly coinciding with the FRE, as shown in Fig. 2a.

3.2. Characterization of modeled MWs

Fig. 3 shows w' at 600 hPa for the 12 cases that satisfy the criteria applied to define an enhanced presence of MWs (Section 3). As stated in Section 2, $t=0$ indicates FRE during each storm. Clearly, w' remains almost invariable with time in these events. Only cases 1, 4, 7, 9 and 10 show a slight time displacement towards the east, which may be associated with the direction of propagation of the wave (see below). A Morlet Continuous Wavelet Transform (CWT) along the zonal and meridional directions is applied to w' to isolate the dominant spectral components. This allows to infer the zonal and meridional wavelengths λ_x, λ_y and both components of the horizontal wavenumber vector $K_H=(k_x,k_y)$, since $k_x=\frac{2\pi}{\lambda_x}$ and $k_y=\frac{2\pi}{\lambda_y}$. It is possible to estimate the horizontal direction of propagation $\alpha=\arctan\left(\frac{k_y}{k_x}\right)$. The signs of k_x and k_y depend on the direction of the wind. It is well known that the horizontal wavelength (λ_H) is minimum when analyzed along the direction of propagation of the wave (Nappo, 2002). Therefore, if $\alpha\neq 0$, we recalculate the CWT in that direction. In all cases a dominant MWs mode was observed, as recently reported from simulations in the Andes region (de la Torre et al., 2011). Each mode may be characterized as being contained in a wavelength interval. Table 1 summarizes dates, FRE times and a range of λ_H for the 12 storms. FRE time varies between 11Z and 22Z, with more than 50% of the sample distributed in the range 16–19Z and

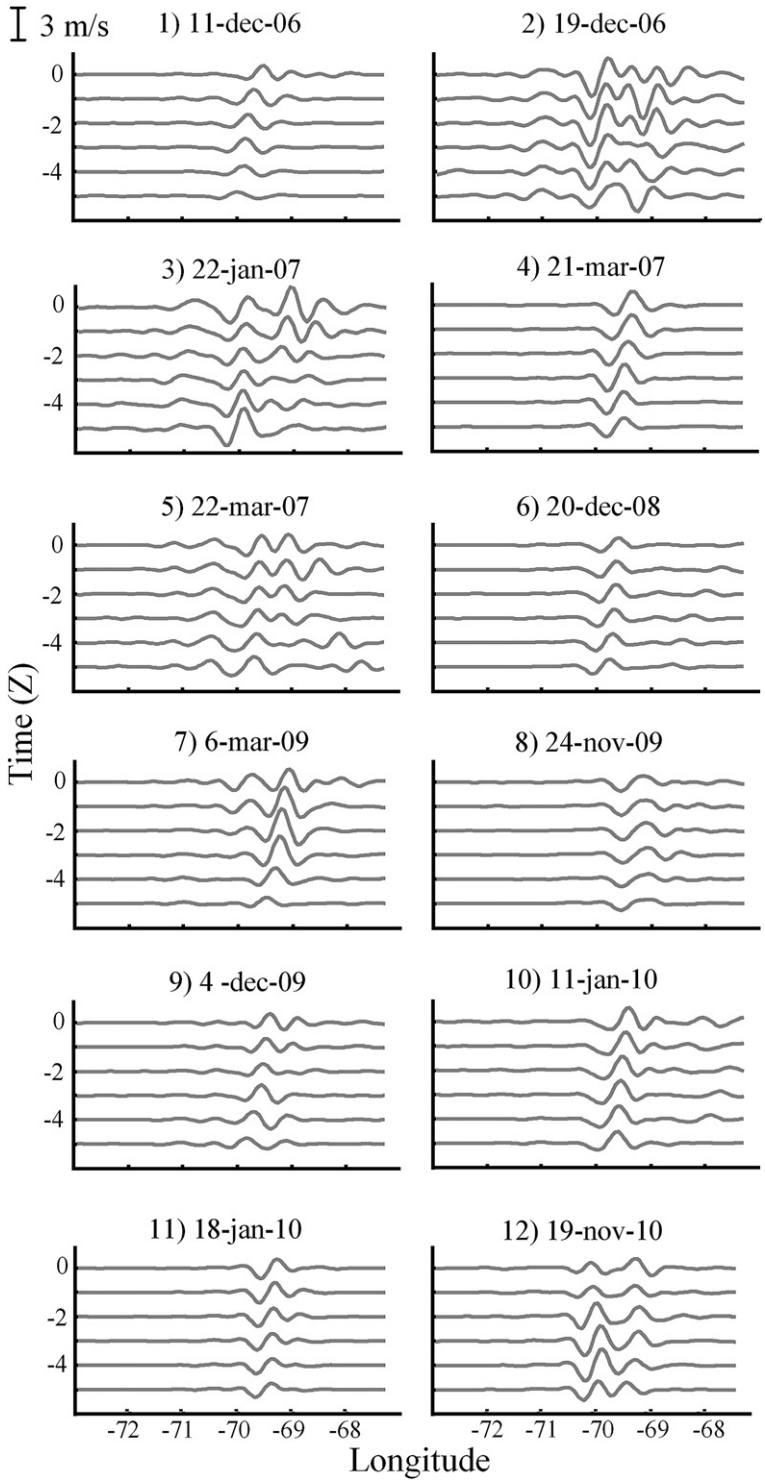

Fig. 3. w' at 600 hPa for M_w, between $t=-5$ and $t=0$ (time of FRE). All cases are performed at latitude of FRE.

almost all are between 16*Z* and 20*Z*. The minimum value for λ_H is 40 km (case 11) and the maximum is 160 km (case 9). A selected case, corresponding to 21 March 2007 (case 4) is illustrated in Fig. 4. The corresponding w' field at 600 hPa, 2 h before FRE, is presented in Fig. 4a, where $\alpha_4=-35°$ was found. The square *S* centered over FRE limits the region verifying the above mentioned criteria for the presence of MW (Section 3). Fig. 4b shows the vertical structure of w' along the direction of propagation (dotted line in Fig. 4a), centered over FRE location. The expected slight westward

tilting with increasing height (Smith (1979)) for a non-hydrostatic MW is observed. Fig. 4c shows the CWT for this case, along α_4. The wavelet coefficients C are calculated by scaling and shifting the wavelet base function ψ (for example, the Morlet) along the signal $f(x)$. If s is the scale and p is the position, then $C(s,p)=\int_{-\infty}^{\infty} f(x)\psi(s,p,x)dx$. The wavelet coefficients represent how closely correlated is $f(x)$ with the scale and shifting (ψ) (Torrence and Compo, 1998). The modeled horizontal wavelength present in this case is shown in Fig. 4c. Colors and intensities indicate the presence of important oscillation modes: it is possible to distinguish one main MW mode of oscillation within the wavelength range $60<\lambda_H<120$. The structure observed in Fig. 4b, allows to estimate the vertical wavelength, obtaining $\lambda_V \sim 7$ km (Mahalov et al., 2011).

3.3. Characterization of observed storms

In this section we describe the following variables derived from radar data: precipitation flux (P), maximum reflectivity (Z), the height top of the cell (h) and the height of the nuclei with maximum reflectivity (H). Precipitation flux is defined by $\int_A z dA$, where $z=200r^{0.6}$ is the radar reflectivity in dBz, A is the cell area in m^2 and r is the rain rate in mm/h. We calculate the median of the four variables, defined as the central member of the population at each time step, instead of the mean in order to avoid possible bias effects. As stated in Section 2, $t=0$ indicates the initial time of each storm. However, since the durations of the events are quite different, the ending times of the periods shown in Fig. 5 do not represent the actual dissipation of the storms. We denote with $\hat{X}_{mw}$ and $\hat{X}_{nomw}$ the median of the generic variable X in the presence (M_w) and absence (NoM_w) of MWs, respectively. The behavior of other parameters of the distributions as the 1st and 4th quintiles is presented in Figure 8. Fig. 5a (upper panel) shows that $\hat{P}_{nomw}$ is higher at an earlier stage than $\hat{P}_{mw}$, both increasing with time during the complete period. At around 120 min, the signals are equal. Before 180 min (t_{180}) $\hat{P}_{mw}$ becomes lower at intervals. This is clearer in the lower panel of Fig. 5a, where the difference between $\hat{P}_{nomw}$ and $\hat{P}_{mw}$ is shown. $\hat{Z}$ is shown in Fig. 5b. In the upper panel, lower values of $\hat{Z}_{mw}$ with respect to $\hat{Z}_{nomw}$ are observed before t_{180}. They are equal at this time and after this, the fluctuations increase. Both signals are filtered to remove fluctuations with periods higher than 60 min (smoothed lines in lower panels) in order to retain effects shorter than one hour, since the whole period consists in 280 min (approximately 4 h and 40 min). While the last part of the signal also seems to be amplified, only slight differences appear before t_{180}. Fig. 5c presents $\hat{h}$. A similar behavior to that described for $\hat{Z}_{mw}$ and $\hat{Z}_{nomw}$ during the last stage of the events is

Table 1
Date of storm, time of FRE and the wavelength range found in the 12 storm cases.

Case	Date	Time	λ_h(km)
1	11 Dec 2006	16Z	60–120
2	19 Dec 2006	19Z	80–130
3	31 Dec 2006	17z	60–140
4	21 Mar 2007	17Z	60–120
5	22 Mar 2007	11Z	60–120
6	20 Dec 2008	17Z	60–140
7	06 Mar 2009	20Z	60–100
8	24 Nov 2009	22Z	60–100
9	04 Dec 2009	19Z	80–160
10	11 Jan 2010	17Z	40–100
11	11 Jan 2010	20Z	40–80
12	19 Nov 2010	20Z	60–140

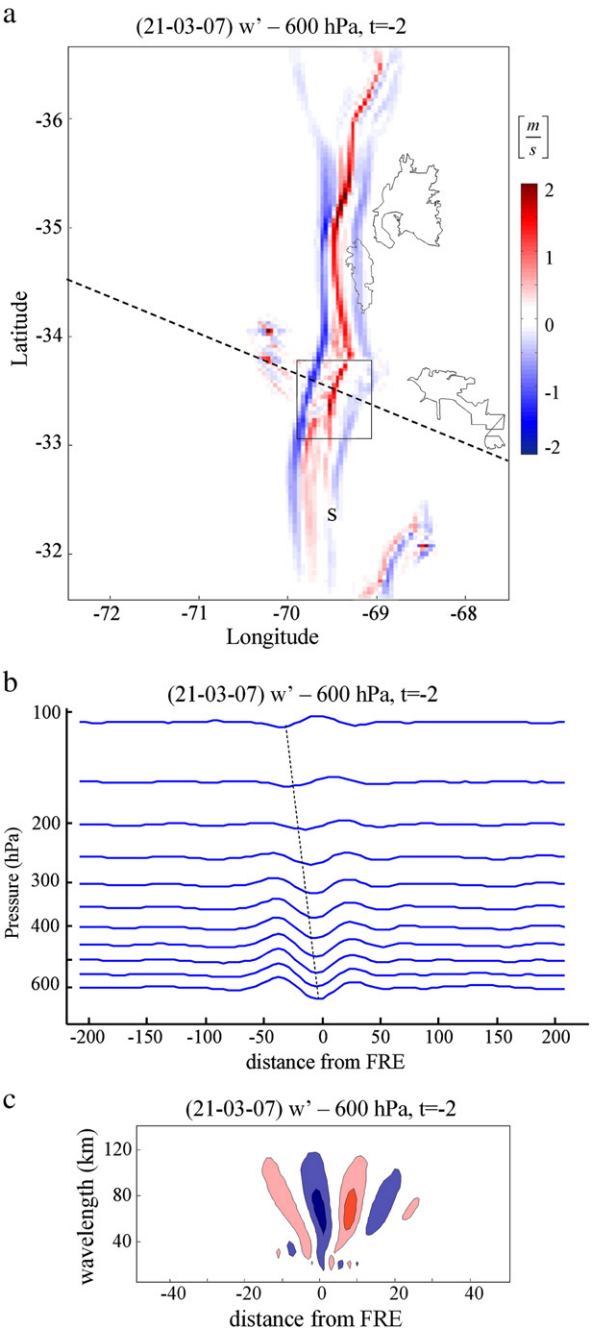

Fig. 4. a) w' at 600 hPa, 2 h before the FRE ($t=-2$) for 21 March 2007. The square "S" indicates the area which verified the criterion of MW existence (see text). Dashed line indicates the direction of propagation (α_4) found in this case; b) w' along α_4 at $t=-2$ for 21-mar-07. c) CWT for w' at $t=-2$ (600 hPa) along α_4 for 21 March 2007.

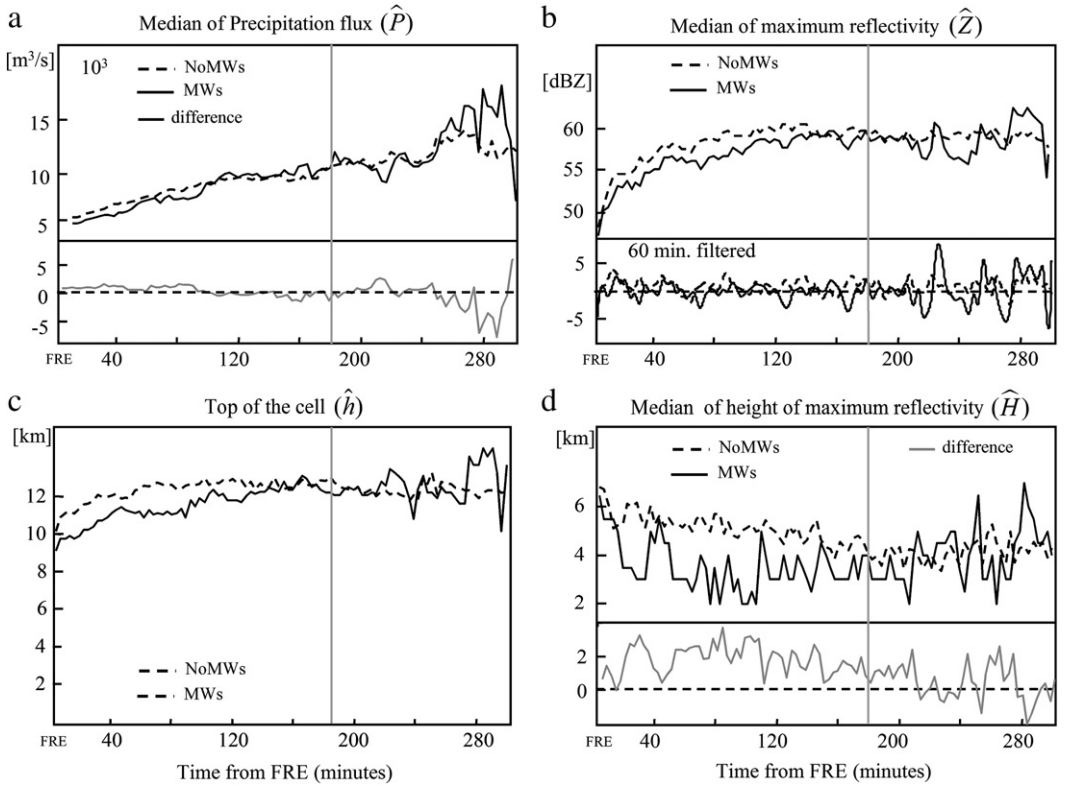

Fig. 5. a) Upper panel: $\hat{P}$ for M_w ($\hat{P}_{mw}$), and NoM_w ($\hat{P}_{nomw}$) starting at FRE time up to 300 min after FRE; lower panel: $\hat{P}_{nomw}-\hat{P}_{mw}$ during the same period; b) upper panel: $\hat{Z}$ for M_w and NoM_w; lower panel: both signals high-pass filtered with cutoff = 60 min; c) idem upper panel a) but for the top of the cell ($(\hat{h})$). d) Idem a) but for the height of the nuclei of maximum reflectivity ($\hat{H}$). Gray line indicates t_{180} (see text).

evident. $\hat{H}$ is shown in Fig. 5d. There is a remarkable difference between the median of the two samples, where $\hat{H}_{mw}$ is lower than $\hat{H}_{nomw}$. It is observed from Fig. 5b that around 40–60 min the 55 dBz level is already reached. At this time, Fig. 5d shows $\hat{H}_{mw}$ and $\hat{H}_{nomw}$ around 4 and 6 km, respectively. There is a general decrease (uniform) behavior of $\hat{H}_{nomw}(\hat{H}_{mw})$. However, both samples present high values of reflectivity during the complete period (Fig. 5b). All parameters change the observed behavior between M_w and NoM_w near t_{180} (gray line in Fig. 5). It is possible to associate the behavior observed in $\hat{Z}$ (Fig. 5b) after t_{180} to a stationary wave with intrinsic period around 40 min capable of driving storm cells up and down during their displacement. For both samples there is a general increase in $\hat{P}$ with time (Fig. 5a), values of $\hat{Z}$ exceeding 50–55 dBz (Fig. 5b) and $\hat{h}$ higher than 10 km (Fig. 5c), respectively. As mentioned in Section 1, these values are experimentally found to be indicators of the presence of hail. On the other hand, López and Sánchez (2009) stated that a time–height plot of the vertical reflectivity profile in the storm allows to see that when the hail begins to fall down the reflectivity decreases accordingly (i.e. change of state from liquid to solid and the elevated hail core in the storm falling to the ground). The $\hat{H}$ features in addition with those described in the others variables, could be indicating that in presence of MWs the hail precipitation occurs at an early stage of the storm evolution and may be stronger in M_w compared with NoM_w. From FRE position as a reference and following the procedure described in Section 2, the storm cell speed and direction of displacement are determined. Fig. 6a and b shows the mean of this variable for NoM_w (solid) and M_w (dashed), respectively. We found $\beta = (27 \pm 26)°$ and $\beta = (2 \pm 15)°$, with a median of 28° and 6.5°, respectively. Although the number of cases for NoM_w is almost twice as large as M_w, the dispersion is lower in the last case. The mean of the displacement speed obtained for each storm is presented in Fig. 6b. M_w is clearly faster than NoM_w, although it is not possible to establish if both samples belong to populations with different means. The mean value of M_w is located outside of the $mean \pm SD$ zone for NoM_w. The two extreme directions of displacement given in Table 2 are plotted with arrows in Fig. 6, which schematizes these results through their average values.

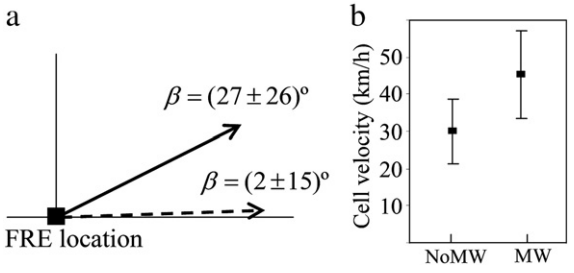

Fig. 6. a) mean angle β of NoM_w (solid) and M_w (dashed); b) velocity of displacement averaged for NoM_w and M_w.

Table 2
Storm cell speed and direction of displacement for NoM_w and M_w.

NoM_w	Dir	$s\left(\frac{km}{h}\right)$	M_w	Dir	$V\left(\frac{km}{h}\right)$
03 Nov 2006	5°	40	11 Dec 2006	9°	22
12 Dec 2006	−16°	16	19 Dec 2006	11°	47
31 Dec 2006	15°	34	22 Jan 2007	−16°	45
26 Jan 2007	28°	30	21 Mar 2007	−1°	46
28 Jan 2007	28°	21	22 Mar 2007	−32°	56
25 Feb 2007	39°	39	20 Dec 2008	−1°	40
20 Jan 2008	37°	28	06 Mar 2009	30°	53
05 Dec 2008	70°	30	24 Nov 2009	−12°	71
07 Dec 2008	17°	25	04 Dec 2009	4°	39
09 Dec 2008	−4°	41	11 Jan 2010	16°	51
08 Dec 2008	−8°	29	11 Jan 2010	11°	26
10 Dec 2009	27°	40	19 Nov 2010	15°	35
11 Dec 2009	26°	15			
15 Dec 2009	42°	38			
17 Dec 2009	27°	36			
31 Dec 2009	34°	30			
03 Jan 2010	41°	34			
22 Jan 2010	60°	28			
26 Jan 2010	−15°	17			
28 Jan 2010	−6°	36			
18 Feb 2010	−17°	48			
18 Nov 2010	57°	27			
28 Nov 2010	54°	37			
15 Feb 2011	36°	18			
22 Feb 2011	−89°	30			
06 Mar 2011	63°	21			
10 Mar 2011	37°	21			

3.4. Energy of modeled MWs

Following the procedure employed by de la Torre et al. (2011), we now compare the vertical kinetic energy provided by M_w, against the energy necessary to develop deep convection events. For this purpose, we evaluate two instability indices: Convective Available Potential Energy (*CAPE*) and Convective Inhibition (*CIN*). As mentioned in Section 1, *CAPE* represents the buoyancy available to rising air parcels (e.g. Emanuel, 1994) although it is well known (e.g. Riemann-Campe et al., 2009) that high *CAPE* values do not necessarily lead to strong convection. From its traditional definition, (e.g. Emanuel, 1994):

$$CAPE = \int_{LFC}^{NBL} g.\frac{T_{v(par)} - T_{v(env)}}{T}_{v(env)} dz \quad (1)$$

where *LFC*, *NBL* and $Tv_{(par/env)}$ are the level of free convection, the neutral buoyancy level and the virtual temperature of the selected parcel and environment, respectively. Following the last definition,

$$CIN = \int_{ILL}^{LFC} g\frac{T_{v(par)} - T_{v(env)}}{T}_{v(env)} dz \quad (2)$$

CIN describes a stable surface layer, which rising air parcels have to overcome to reach the unstable layer: In this last equation, *ILL* represents an initial lower level for the selected parcel. Fig. 7a and b depicts the median and mean of *CAPE* and *CIN* over an area of 100×100 km around FRE position, for NoM_w and M_w from $t=-4$ up to one hour after FRE time. Since the surface of San Rafael is not at sea level but above 850 hPa, we consider *CAPE* and *CIN* for a parcel at 800 hPa. Thus, T_{800} from WRF simulations is used in Eqs. (1) and (2). Fig. 7a and b shows that *CAPE* is rather weak in both samples, although larger during M_w. *CIN* in both samples evidences the inhibition of energy needed (or required) to be overcome for convection development. *CAPE* for M_w exhibits an increase with time from $t=-4$ up to $t=-1$, while for this sample *CIN* stands near -2 m^2/s^2 from $t=-4$ to -2 and becomes lower in absolute value close to FRE time. In Fig. 7c the mean kinetic energy (K_E) (corresponding to M_w), defined as $K_E = \frac{(w')^2}{2}$ at 800 hPa, is compared at one hour intervals with the simulated *CIN*. After $t=-3$, K_E is higher than *CIN* in absolute value, evidencing that there is enough energy available to overcome the stable layer. The non-dimensional number $\frac{K_E}{|CIN|}$ (mean values) is shown in Fig. 7d (solid line). From $t=-1$ this quantity presents a slow increase and then grows up to FRE time value. This effect could be associated to the almost constant K_E related with a decreasing |*CIN*| (Fig. 7c). The ratio $\frac{CAPE}{|CIN|}$ (Miglietta and Rotunno, 2009) shows constant value between $t=-4$ and $t=-1$ and becomes higher after $t=-1$ (dotted line in Fig. 7d). During the FRE time, a strong decrease is present in this quantity, probably associated to the decreasing in *CAPE* while *CIN* remains almost constant. These features could be indicating that close to the FRE time, the instability grows and although a stable layer is inhibits the convection development, there is enough kinetic energy provided by the MWs able to overcome it.

4. Conclusions

39 severe storm cases were found over the orographic region of Mendoza, Argentina during 2006–2010 period. The storm geneses locations are almost aligned with the regional topography, which presents a systematic decrease downwind to the mean flow. From Favorable Areas of Convective Development index (FACD) it was possible to determine that the numerical model is able to detect the convection over the study area, coinciding roughly with the FRE observed. The simulated *w* for these events shows a stationary behavior of the main modes in 12 of them. Two samples with mountain waves (M_w) and without mountain waves (NoM_w) were analyzed. From radar data, the observed behavior of precipitation flux, maximum reflectivity, the height top of the cell and the height of the nuclei with maximum reflectivity from the two samples, changes near t_{180} in all parameters. After this time, it is possible to distinguish a stationary wave with intrinsic period around 40 min capable of driving the cells up and down during their displacement. Stationary modes which presented variations of λ_H between 40 and 160 km and a direction of propagation between −32° and 30° were determined for M_w. The vertical wavelength estimated for these structures is ~7 km. The direction of storm displacement is given by the mean flow in the two samples. However, differences between them are found: NoM_w shows more variability than M_w and the mean direction has a stronger northern component (27°) with respect to M_w (2°). From the mean cell storm speed of both samples, it is clear that M_w is faster. The ratio $\frac{CAPE}{|CIN|}$ shows a constant value between $t=-4$ and $t=-1$ and becomes higher after $t=-1$. However, the

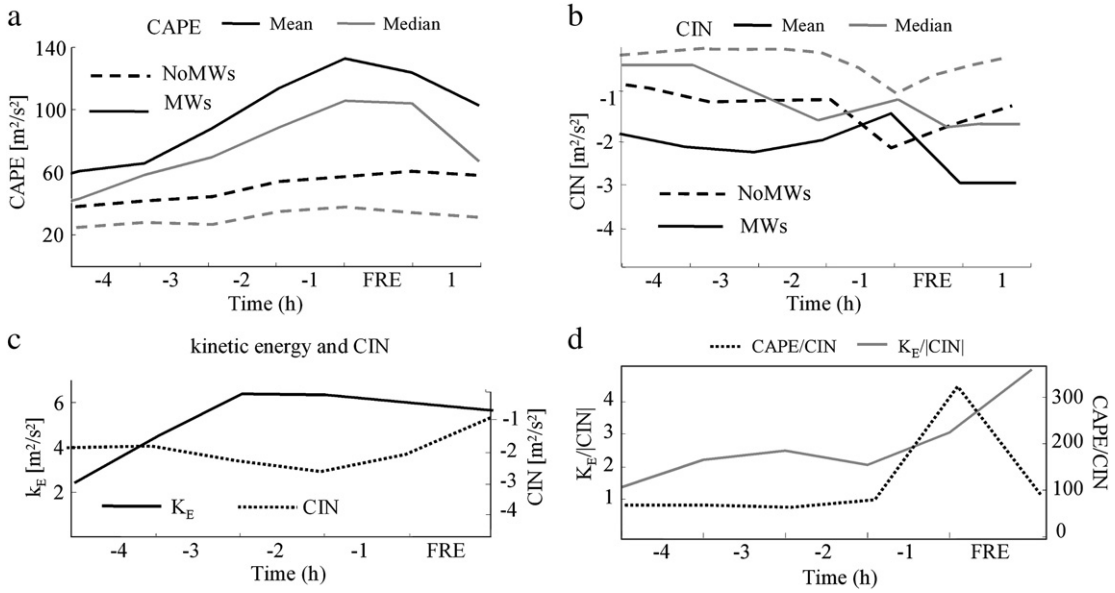

Fig. 7. a) and b) mean (dark) and median (gray) of *CAPE* and *CIN* averaged for NoM_w (dashed) and M_w (solid) at 800 hPa, respectively. Initial time is 4 h before FRE time ($t=-4$) and final time 1 h after ($t=1$); c) kinetic energy ($K_E=\frac{(w')^2}{2}$) (solid line) and *CIN* (dotted) averaged for M_w; d) $\frac{K_E}{CIN}$ (solid) and $\frac{CAPE}{CIN}$ (dotted) averaged for M_w at 800 hPa.

stable layer present and detected by the *CIN* values, may be exceeded by the energy provided by the MWs. This requirement seems to be fulfilled: (i) since from $t=-3$, the kinetic energy associated to the waves is higher than the *CIN* in absolute value, keeping this behavior up to the FRE and (ii) the non-dimensional number $\frac{K_E}{|CIN|}$ which relates the kinetic

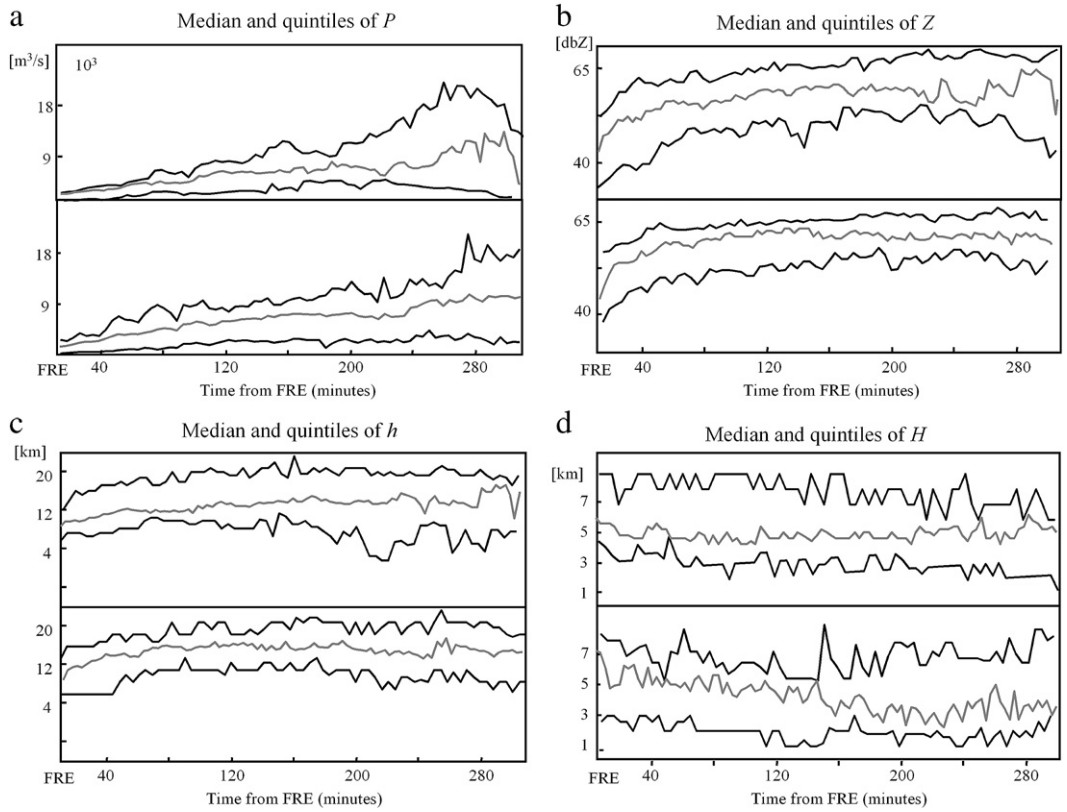

Fig. 8. Idem Fig. 5 but showing the 1st and 4th quintiles (dark) and median (gray). Upper panel for M_w and lower panel for NoM_w.

energy provided by M_w with *CIN*, shows that after $t=-4$ there is enough energy to overcome this layer.

Appendix A

Fig. 8 shows the 1st quintile, the 4th quintile and the median for the variables discussed in Section 2. The upper panel correspond to M_w and the lower to NoM_w. Dark lines indicate the behavior of the 1st and 4th quintiles and the gray lines indicate the median for each case. *P* (Fig. 8a) shows an increase between the two quintiles along the whole period. This difference is more clear before $t\sim200$ min and is stronger for M_w. These statistics for *Z* (Fig. 8b) show a different behavior: for M_w the difference between the 1st and 4th quintiles remains pretty constant up to $t=180$ min and increases later, while in NoM_w the difference remains rather constant with time. The top of the cell (*h*) shows similar regimes respect to *Z* for M_w and NoM_w. In both cases, the difference between 1st and 4th quintiles increases with time before $t\sim180$ min.

References

Brooks, H.E., Doswell III, C.A., Kay, M.P., 2003. Climatological estimates of local daily tornado probability for the United States. Weather Forecast. 18, 626–664.

Colby, Frank P., 1984. Convective inhibition as a predictor of convection during AVE-SESAME II. Mon. Weather Rev. 112, 2239–2252.

de la Torre, A., Vincent, D., Tailleaux, R., Teitelbaum, H., 2004. A deep convection event above the Tunuyán Valley near to the Andes Mountains. Mon. Weather Rev. 132 (9), 2259–2268.

de la Torre, A., Alexander, P., Llamedo, P., Menéndez, C., Schmidt, T., Wickert, J., 2006. Gravity waves above the Andes detected from GPS radio occultation temperature profiles: jet mechanism? Geophys. Res. Lett. 33, L24810 http://dx.doi.org/10.1029/2006GL027343.

de la Torre, A., Hierro, R., Llamedo, P., Rolla, A., Alexander, P., 2011. Severe hail storms near southern Andes in the presence of mountain waves. Atmos. Res. 101 (1–2), 112–123 http://dx.doi.org/10.1016/j.atmosres.2011.01.015.

Dixon, M., Wiener, G., 1993. TITAN: thunderstorm identification, tracking, analysis and nowcasting, a radar-based methodology. J. Atmos. Oceanic Technol. 10, 785–797.

Donavon, R.A., Jungbluth, K.A., 2007. Evaluation of a technique for radar identification of large hail across the Upper Midwest and Central Plains of the United States. Weather Forecast. 22, 244–254.

Dudhia, J., 1989. Numerical study of convection observed during the winter monsoon experiment using a mesoscale two-dimensional model. J. Atmos. Sci. 46, 3077–3107.

Eckermann, S.D., Preusse, P., 1999. Global measurements of stratospheric mountain waves from space. Science 286, 1534–1537.

Emanuel, K.A., 1994. Atmospheric Convection. Oxford University Press, New York . 580 pp.

Fraile, R., Castro, A., Sánchez, J.L., Marcos, J.L., López, L., 2001. Noteworthy C-band radar parameters of storms on hail days in northwestern Spain. Atmos. Res. 59-60, 41–61.

Galway, J.G., 1956. The lifted index as a predictor of latent instability. Bull. Am. Meteorol. Soc. 37, 528–529.

García-Ortega, E., López, L., Sánchez, J.L., 2009. Diagnosis and sensitivity study of two severe storm events in the Southeastern Andes. Atmos. Res. 93, 161–178.

George, J.J., 1960. Weather and Forecasting for Aeronautics. Academic Press, pp. 410–415.

Grell, G.A., Devenyi, D., 2002. A generalized approach to parameterizing convection combining ensemble and data assimilation techniques. Geophys. Res. Lett. 29 http://dx.doi.org/10.1029/2002GL015311.

Hong, S.-Y., Dudhia, J., Chen, S.-H., 2004. A revised approach to ice microphysical processes for the bulk parameterization of cloud and precipitation. Mon. Weather Rev. 132, 103–120.

Hong, S.-Y., Noh, Y., Dudhia, J., 2006. A new vertical diffusion package with an explicit treatment of entrainment processes. Mon. Weather Rev. 134, 2318–2341.

Houze Jr., R.A., 1993. Cloud Dynamics. Academic Press, New York, USA.

Houze Jr., R.A., 2012. Orographic effects on precipitating clouds. Rev. Geophys. 50, RG1001 http://dx.doi.org/10.1029/2011RG000365.

Johns, R.H., Doswell III, C.A., 1992. Severe local storms forecasting. Weather Forecast. 7, 588–612.

Lemon, L.R., 1980. Severe thunderstorm radar identification techniques and warning criteria. NOAA Tech. Memo. NWS NSSFC-3. 60 pp.

López, L., Sánchez, J.L., 2009. Discriminant methods for radar detection of hail. Atmos. Res. 93, 358–368.

López, L., García-Ortega, E., Sánchez, J.L., 2007. A shortterm forecast model for hail. Atmos. Res. 83, 176–184.

Mahalov, A., Moustaoui, M., Grubiic, V., 2011. A numerical study of mountain waves in the upper troposphere and lower stratosphere. Atmos. Chem. Phys. 11, 5123–5139 http://dx.doi.org/10.5194/acp-11-5123-2011.

Miglietta, M.M., Buzzi, A., 2004. A numerical study of moist stratified flow regimes over isolated topography. Q. J. R. Meteorol. Soc. 130, 1749–1770 http://dx.doi.org/10.1256/qj.02.225.

Miglietta, M.M., Rotunno, R., 2009. Numerical simulations of conditionally unstable flows over a ridge. J. Atmos. Sci. 66, 1865–1885.

Miller, R.C., 1967. Notes on analysis and severe storm forecasting procedures of the Military Weather Warning Center. AWS Tech. Rep. 200. 94 pp. [Headquarters, AWS, Scott AFB, 1L 62225].

Mlawer, E.J., Taubman, S.J., Brown, P.D., Iacono, M.J., Clough, S.A., 1997. Radiative transfer for inhomogeneous atmosphere: RRTM, a validated correlated-k model for the long-wave. J. Geophys. Res. 102 (D14), 16663–16682.

Moncrieff, M.W., Miller, M.J., 1976. The dynamics and simulation of tropical cumulonimbus and squall lines. Q. J. R. Meteorol. Soc. 102, 373–394.

Monin, A.S., Obukhov, A.M., 1954. Basic laws of turbulent mixing in the surface layer of the atmosphere. Trans. Geophys. Inst. Akad. Nauk. USSR 151, 163–187.

Nappo, C.J., 2002. An introduction to atmospheric gravity waves. Int. Geophys. Ser., 85. Academic, San Diego, California . 276 pp.

Riemann-Campe, K., Fraedrich, K., Lunkeit, F., 2009. Global climatology of 631 convective available potential energy (CAPE) and convective inhibition 632 (CIN) in ERA-40 reanalysis. Atmos. Res. 93, 534–545.

Sánchez, J.L., García, E., Marcos, J.L., Dessens, J., 1999. Proceedings of the EGS Plinius Conference held at Maratea, October, Italy.

Sánchez, J.L., López, L., Bustos, C., Marcos, J.L., García-Ortega, E., 2008. Short-term forecast of thunderstorms in Argentina. Atmos. Res. 88, 36–45.

Schneidereit, M., Schär, C., 1999. Idealised numerical experiments of Alpine flow regimes and Southside precipitation events. Meteorol. Atmos. Phys. 72, 233–250.

Showalter, A.K., 1953. A stability index for thunderstorm forecasting. Bull. Am. Meteorol. Soc. 34, 250–252.

Shutts, G.J., Kitchen, M., Hoare, P.H., 1988. A large amplitude gravity wave in the lower stratosphere detected by radiosonde. Q. J. R. Meteorol. Soc. 114, 579–594.

Skamarock, W.C., Klemp, J.B., Dudhia, J., Gill, D.O., Barker, D.M., Duda, M., Huang, X.-Y., Wang, W., Powers, J.G., 2008. A description of the advanced research WRF version 3. NCAR Technical Note NCAR/TN-475+STR.

Smith, R.B., 1979. The influence of mountains on the atmosphere. Adv. Geophys. 21, 87–230.

Torrence, C., Compo, G.P., 1998. A practical guide to wavelet analysis. Bull. Am. Meteorol. Soc. 79, 6178.

Williams, E., Renno, N., 1992. An analysis of the conditional instability of the tropical atmosphere. Mon. Weather Rev. 121 (1), 21–36.